

Influence of geometrical parameters on the strength of Hybrid CFRP-aluminium tubular adhesive joints

Lavalette, Nicolas P.; Bergsma, Otto K.; Zarouchas, Dimitrios; Benedictus, Rinze

DOI

[10.1016/j.compstruct.2020.112077](https://doi.org/10.1016/j.compstruct.2020.112077)

Publication date

2020

Document Version

Final published version

Published in

Composite Structures

Citation (APA)

Lavalette, N. P., Bergsma, O. K., Zarouchas, D., & Benedictus, R. (2020). Influence of geometrical parameters on the strength of Hybrid CFRP-aluminium tubular adhesive joints. *Composite Structures*, 240, Article 112077. <https://doi.org/10.1016/j.compstruct.2020.112077>

Important note

To cite this publication, please use the final published version (if applicable). Please check the document version above.

Copyright

Other than for strictly personal use, it is not permitted to download, forward or distribute the text or part of it, without the consent of the author(s) and/or copyright holder(s), unless the work is under an open content license such as Creative Commons.

Takedown policy

Please contact us and provide details if you believe this document breaches copyrights. We will remove access to the work immediately and investigate your claim.



Influence of geometrical parameters on the strength of Hybrid CFRP-aluminium tubular adhesive joints

Nicolas P. Lavalette*, Otto K. Bergsma, Dimitrios Zarouchas, Rinze Benedictus

Department of Aerospace Structures and Materials, Faculty of Aerospace Engineering, Delft University of Technology, Kluyverweg 1, 2629HS Delft, The Netherlands

ARTICLE INFO

Keywords:

Adhesive joints
Tubular joints
Hybrid joints
Ductile adhesives
Cohesive zone modelling
Mechanical testing

ABSTRACT

Tubular adhesive joints, used in truss structures to join pultruded carbon fibre-reinforced polymer members to aluminium nodes, are modelled with varying dimensions. The numerical model uses a Cohesive Zone Modelling formulation with a trapezoidal traction-separation law for the adhesive layer, and experimental tests are carried out to validate it. The results showed that the joint strength increases significantly with the bonding area, with a limit on the overlap length above which it stops increasing. This upper limit is affected by the thickness and tapering angle of the adherends, due to their influence on the shear stress distribution along the overlap. On the other hand, the adhesive thickness has only a marginal influence on the joint strength.

1. Introduction

Composite materials are increasingly used in transportation industries, due to their low weight and high mechanical properties. Truss structures, which consist of straight members loaded axially and connected together by nodes, are a suitable application for the high axial strength of unidirectional composite materials, such as carbon fibre-reinforced polymer (CFRP) pultrusions, and several applications of CFRP used in truss structures are being developed in the form of wound trusses and lattices [1–3]. A limitation to such structures is the load transfer between the members, therefore designing the nodes is an important step in designing the overall structure. The efficiency of a node is defined as the ratio of the load it can transfer to the load the members can carry. Mechanical fastening, such as riveting, provides a high efficiency but damages composite materials. In addition, it is difficult to apply to small-scale structures without significantly increasing their total weight. A solution is to adhesively bond the ends of the members to the nodes, as it can provide strengths comparable to or higher than mechanical fastening [4–6]. In a previous work, the authors simulated the strength of different node configurations and concluded that tubular joints, consisting of aluminium sockets overlapping the truss members, provided the best strength-to-weight ratio [7].

The dimensions of adhesive joints play a crucial role in their strength. Increasing the bonding area, i.e. the overlap length and width, greatly contributes to increasing the joint strength [8–12]. To a lower extent, an increase of the joint strength can be obtained by increasing

the adherends thickness, which causes a higher bending stiffness [9,13]. Tapering the ends of the adherends also results in an increase of the joint strength by making the stress distribution in the adhesive more uniform [14], although this effect is marginal on tubular joints [15,16]. Additionally, tubular joints present a good robustness to manufacturing defects, such as bondline contamination or misalignment of the tubes relative to each other [17,18]. Increasing the adhesive bondline thickness can cause a reduction of the joint strength, although no generalized trend has been observed due to the numerous factors that can influence it [19,20]. The joint strength also depends on the type of adhesive used. Brittle adhesives generally have a higher strength than ductile adhesives, but their sensitivity to peak stresses limits this advantage to short overlaps, for which the stress distributions are more uniform [21,22]. Ductile adhesives plasticize when their peak strength is reached, and thereby redistribute the stresses in the less loaded parts of the overlap, which results in a higher performance than brittle adhesives for longer overlaps [23,24]. Knowing the influence of the geometrical parameters on the strength and weight of a joint is necessary to design and optimize it, since strength and weight objectives in this case are often of conflicting nature [15]. In particular, it is important to determine the design limits of each parameter, outside which no further strength or weight improvement is possible.

In order to determine these limits, a model able to predict the strength of the adhesive joint is required. Analytical models exist to analyse the stress distribution and predict the failure of adhesive joints, but they are not reliable for the modelling of adhesive displaying a

* Corresponding author.

E-mail addresses: n.p.lavalette@tudelft.nl (N.P. Lavalette), o.k.bergsma@tudelft.nl (O.K. Bergsma), d.zarouchas@tudelft.nl (D. Zarouchas), r.benedictus@tudelft.nl (R. Benedictus).

<https://doi.org/10.1016/j.compstruct.2020.112077>

Received 4 December 2019; Received in revised form 5 February 2020; Accepted 14 February 2020

Available online 17 February 2020

0263-8223/ © 2020 The Authors. Published by Elsevier Ltd. This is an open access article under the CC BY license (<http://creativecommons.org/licenses/by/4.0/>).

highly non-linear behaviour, in which case numerical models are preferred [25,26]. Finite Element Modelling (FEM) has been used extensively to analyse adhesive bonds and predict their strength, using a variety of criteria to determine the failure of the joint. The criteria to be used depend on the geometry of the joint (lap, scarf, etc.), and on the type of adhesive used, with local stress-strain criteria being generally more suitable for brittle adhesives and global yielding criteria giving more accurate results for ductile adhesives [24,27–29]. With the increase in computational power, more advanced modelling techniques are now being used, such as fracture mechanics and damage modelling, which comprise Cohesive Zone Modelling (CZM) and Extended Finite Element Method (XFEM) [30,31,32]. In the case of ductile adhesives, fracture mechanics are not suitable because the initial crack size and position is difficult to determine, and would require a large amount of computing time [29]. CZM combines the advantages of fracture and continuum mechanics to model the damage initiation and propagation through the adhesive layer until failure, and has been successfully used in the literature to predict the strength of adhesive joints. Even though XFEM shows satisfactory results compared to standard FEM, it has shown limited and less accurate results in the strength prediction of adhesive joints compared to CZM [20,21,33]. The choice of the traction-separation law to be used for the CZM depends on the adhesive. A triangular law, which models the stiffness degradation of the material immediately after damage initiation, shows more accurate results for brittle adhesives, while a trapezoidal law, by representing the plasticization of the material, is more suited to ductile adhesives [22].

The objective of the present work is to study the influence of several geometrical parameters on the strength of CFRP-aluminium tubular joints, in order to determine the limits of each parameter in improving the joint strength and weight and assess their relevance for a future optimization process. The parameters considered are the overlap length (L_o), adhesive thickness (t_{adh}), inner tube diameter (d_{in}), inner and outer tubes thickness (t_{in} and t_{out} , respectively), and inner and outer tubes taper lengths (l_{in} and l_{out} , respectively), as their influence on the joint strength and weight is expected to be significant. Considering the range of overlap length values, a ductile adhesive (Araldite 2015-1) is chosen, since a brittle adhesive is expected to result in lower strengths in most cases. A numerical model using CZM with a trapezoidal traction-separation law is built to predict the joint strength for varying parameter values. Tubular joints specimens are manufactured and tested in tension until failure for a selection of geometrical parameters, and validation of the numerical model is made by comparing the failure load predictions with those obtained experimentally. In addition, Computed Tomography (CT) scan images of a selection of specimens are made, in order to assess the importance of manufacturing defects on the joint strength and adapt the numerical model if necessary.

2. Methodology

2.1. Material properties

The inner tubes of the joints are unidirectional pultruded tubes composed of TORAYCA® T700 fibres and epoxy resin. The outer tubes are made of aluminium 6086-T6. The properties of the CFRP and aluminium, to be implemented in the numerical model, were calculated from the manufacturers' data. They are disclosed in Tables 1 and 2, respectively.

In order for the numerical models to predict the behaviour of the adhesive joint accurately using CZM, the elastic moduli, failure

Table 2
Properties of the aluminium 6086-T6.

Young's modulus, E^{al} [GPa]	69
Yield strength, σ_y^{al} [MPa]	270
Failure strength, σ_f^{al} [MPa]	330
Failure strain, ϵ_f^{al} [%]	9.8
Poisson's ratio, ν^{al}	0.33

strengths and fracture toughness of the adhesive, in tension and shear, are needed. The adhesive used in this work is the Araldite® 2015-1, a two-component (resin and hardener) ductile epoxy adhesive. It is a new version of the discontinued Araldite® 2015. As reported by the manufacturer (Huntsman International LLC), it shows slightly better performances than its predecessor did. The properties of the Araldite® 2015-1 to be used for the CZM are not expected to vary significantly from those of the Araldite® 2015, which has previously been characterized in the literature [34]. However, Campilho et al. [22] have shown that variations of the adhesive failure strength have a substantial impact on the failure load of the joint predicted by the CZM (up to 20% for a strength variation of 20%), while variations of the fracture toughness only have a marginal impact (up to 5% for a toughness variation of 20%). In order to increase the reliability of the model predictions, the elastic moduli and failure strengths of the Araldite® 2015-1, in tension and shear, are determined experimentally in this work, while its fracture toughness in tension and shear are considered identical to those previously determined for the Araldite® 2015.

Bulk adhesive specimens were tested to determine the tensile properties and Thick Adherent Shear Tests (TAST) were carried out to determine the shear properties. The bulk adhesive specimens were manufactured according to the ISO 15166-1 standard. The adhesive was cured at room temperature for five days between two plates coated with a release agent, with 2 mm thick spacers ensuring a constant adhesive thickness. The resulting adhesive plates were then machined to achieve the dogbone shape specified in the standard, as shown in Fig. 1a. Seven specimens were tested and the tensile properties of the adhesive were determined according to the ISO 527-2 standard. The TAST specimens were manufactured according to the ISO 11003-2:201 standard. Two steel plates were degreased with acetone, manually abraded using sandpaper and bonded together, with spacers guaranteeing an overlap thickness of 0.5 mm. After curing at room temperature for five days, the bonded assembly was machined to obtain specimens as specified in the standard, as shown in Fig. 1b. Instead of using an extensometer as suggested in the standard, Digital Image Correlation (DIC) was used to measure the displacement of the adherends relative to each other at the location of the overlap (Fig. 2). Seven specimens were tested with four yielding valid results, the remaining three having failed prematurely due to a misalignment in the testing apparatus. Fig. 3 shows the experimental stress-strain curves obtained from the bulk adhesive and TAST specimens. The properties of the Araldite® 2015-1 are summarized in Table 3, with the yield strengths in tension and shear calculated for a respective plastic strain of 0.2%.

2.2. Numerical model

The tubular joints are modelled for different values of overlap length (L_o), adhesive thickness (t_{adh}), inner tube diameter (d_{in}), inner and outer tubes thickness (t_{in} and t_{out} , respectively), and inner and outer tubes taper lengths (l_{in} and l_{out} , respectively). These parameters, shown in Fig. 4, are independent (the value of each parameter can be varied

Table 1
Properties of the CFRP.

E_{11} [MPa]	E_{22} [MPa]	E_{33} [MPa]	ν_{12}	ν_{13}	ν_{23}	G_{12} [MPa]	G_{13} [MPa]	G_{23} [MPa]
146,066	8320	8320	0.248	0.248	0.234	3135	3135	3371

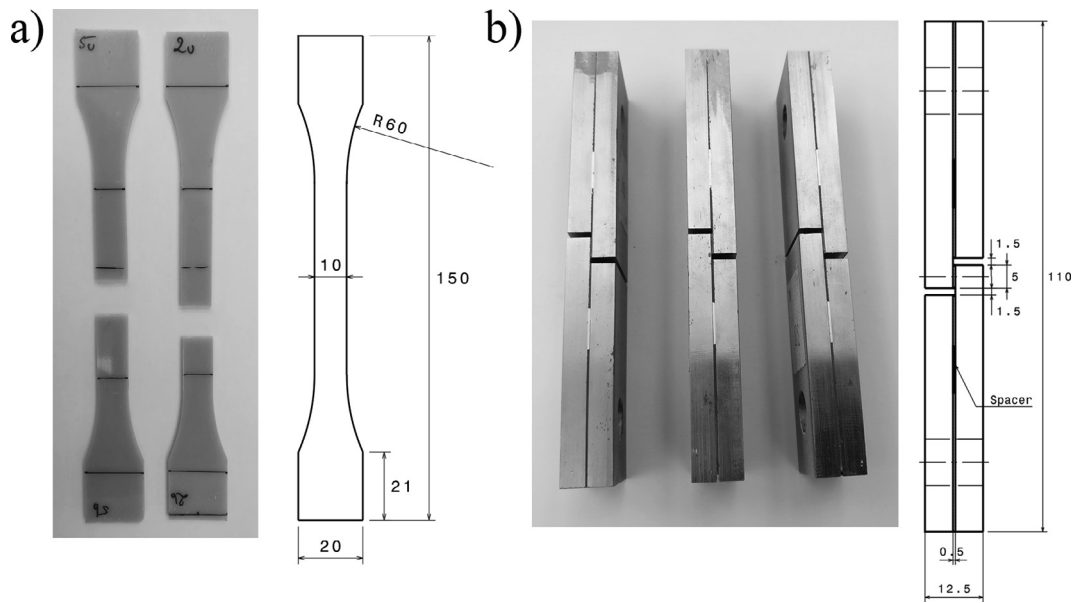


Fig. 1. Examples of bulk adhesive (a) and TAST (b) specimens, manufactured following the ISO 15166-1 and ISO 11003-2:201 standards, respectively.

without affecting the others). In order to represent the specimens used to validate the model as closely as possible, the centring hole and drill tips are also modelled (details about the purpose of the centring hole can be found in Section 2.4).

The numerical model was built and analysed using the Finite Element software Abaqus (Dassault Systèmes). Given the tubular nature of the joints studied, an axisymmetric model was created, as it yields the same results as would a 3D model but with a lower computing time [12]. The adherends were modelled with 4-node axisymmetric quadrilateral elements (CAX4 in Abaqus), using the material properties presented in Tables 1 and 2. CZM can be applied to model the adhesive layer following two different approaches: the “continuum” or the “local” approach. In the continuum approach, the entire adhesive layer is modelled as a single row of cohesive elements acting as an interface of finite thickness between the two adherends. In the local approach, the adhesive is modelled using solid elements, while zero-thickness cohesive elements are inserted at the adhesive-adherends interfaces and within the adhesive layer to simulate different failure paths. For more

details on the two approaches, the readers are referred to Da Silva & Campilho [29]. The continuum approach is used to predict the adhesive bond failure on a macroscopic level and requires a low computational cost, while the local approach allows for a more detailed analysis of the bond failure, for a higher computational cost. Since the objective of this work is limited to predicting the failure load of the tubular joints, the continuum approach was chosen. The adhesive layer was therefore modelled as a single row of 4-node axisymmetric cohesive elements (COHAX4 in Abaqus). A trapezoidal traction-separation law, detailed in Section 2.3, was implemented to model the damage initiation and propagation in the adhesive layer. A convergence study was carried out to determine suitable mesh sizes along the different dimensions, with bias effects applied to create smaller sized elements near the locations of stress concentrations, as shown in Fig. 5. The minimum size for the elements was set to 0.05 mm, and the maximum size to 1 mm. The boundary conditions shown in Fig. 4 were applied to the model to reproduce the testing conditions.

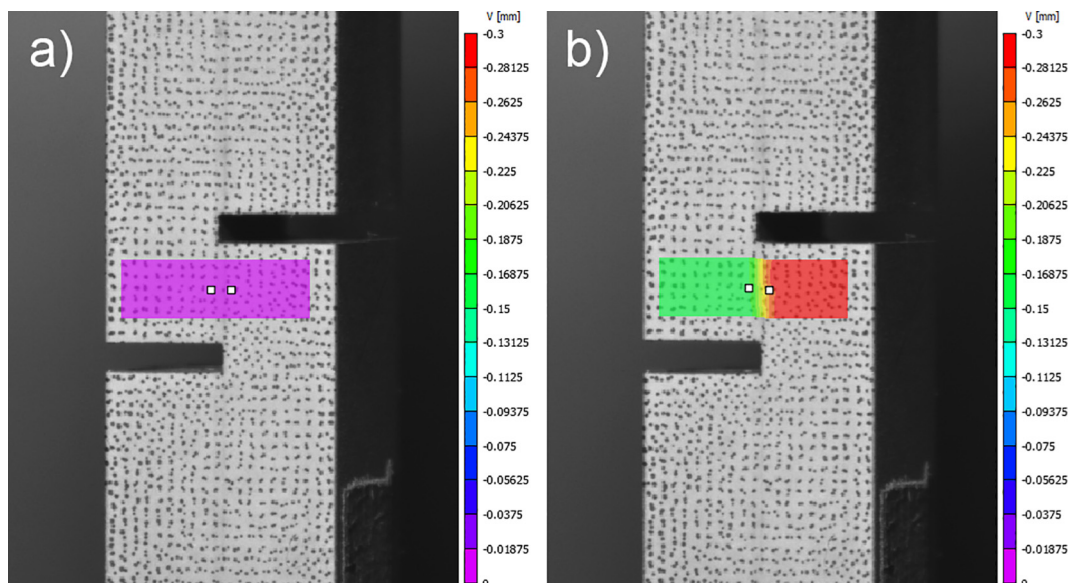


Fig. 2. Vertical displacement measured by DIC around the bonding area of a TAST specimen, before loading (a) and just before failure (b).

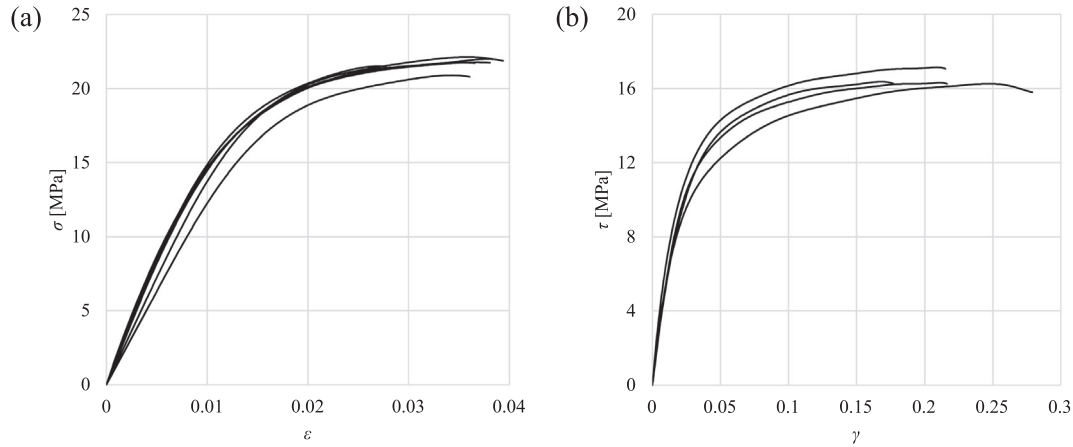


Fig. 3. Experimental stress-strain curves in tension (a) and shear (b) for Araldite 2015-1, obtained from bulk adhesive and TAST specimens, respectively.

Table 3
Properties of the Araldite 2015-1.

Property	Araldite 2015-1
Young's modulus, E [GPa]	1.64 ± 0.22
Tensile yield strength, σ_y [MPa]	15.90 ± 1.19
Tensile failure strength, σ_f [MPa]	21.56 ± 0.51
Tensile failure strain, ϵ_f [%]	3.29 ± 0.53
Shear modulus, G [GPa]	0.67 ± 0.12
Shear yield strength, τ_y [MPa]	6.44 ± 1.03
Shear failure strength, τ_f [MPa]	16.52 ± 0.42
Shear failure strain, γ_f [%]	20.90 ± 3.23
Toughness in tension ^a , G_n^c [N/mm]	0.43 ± 0.02
Toughness in shear ^a , G_s^c [N/mm]	4.70 ± 0.34
Poisson's ratio ^b , ν	0.33

^a Values determined for Araldite 2015 in reference [34].

^b Manufacturer's data.

2.3. CZM implementation

Using the continuum approach, CZM simulates the elastic loading of an adhesive layer followed by local damage initiation and propagation until failure. It is formulated by a traction-separation law, which relates the stresses t and displacements δ between the paired nodes of a cohesive element, in tension and shear. The exact shape of a traction-separation law can be determined experimentally, but requires an extensive testing campaign [35,36]. Approximate laws, such as the triangular and trapezoidal laws shown in Fig. 6, have been shown to give satisfactory results [22,34]. Therefore, the authors decided that using an approximate law was suitable for the purpose of this work. The

choice of a shape to be used for the CZM depends on the adhesive type. Triangular and exponential laws, which model the stiffness degradation of the material immediately after damage initiation, show more accurate results for brittle adhesives, while a trapezoidal law, by representing the plasticization of the material, is more suited to ductile adhesives [22]. In this work, a trapezoidal law is used to represent the behaviour of the Araldite® 2015-1, using the material properties presented in

Table 3 (with t^0 in tension and shear taken as equal to σ_f and τ_f , respectively).

The initial linear elastic behaviour of the adhesive is defined by Eq. (1), where n and s represent tension and shear, respectively.

$$\begin{Bmatrix} t_n \\ t_s \end{Bmatrix} = \begin{bmatrix} K_n & 0 \\ 0 & K_s \end{bmatrix} \begin{Bmatrix} \delta_n \\ \delta_s \end{Bmatrix} \tag{1}$$

K_n and K_s are calculated as the ratios between the elastic stiffness of the adhesive in tension and shear, respectively, and the characteristic length of the adhesive layer, its thickness t_{adh} [37]. The elastic loading of the adhesive is coupled between tension and shear, and damage initiation is considered when the quadratic nominal stress criterion, shown in Eq. (2), is fulfilled. The brackets $\langle \rangle$ indicate that the value is made equal to zero if negative, which prevents compressive stresses from initiating damage.

$$\left(\frac{\langle t_n \rangle}{t_n^0} \right)^2 + \left(\frac{t_s}{t_s^0} \right)^2 = 1 \tag{2}$$

After damage initiation, the adhesive undergoes progressive degradation, characterized by the increase of a damage variable d defined

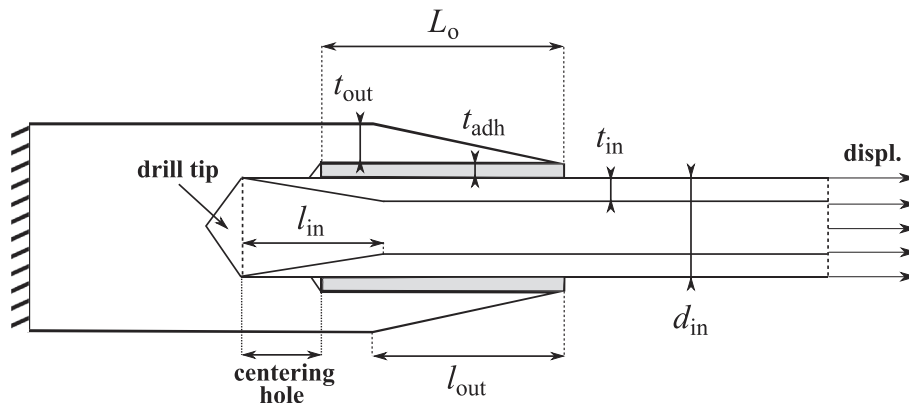


Fig. 4. Dimensions of the tubular joint and boundary conditions.

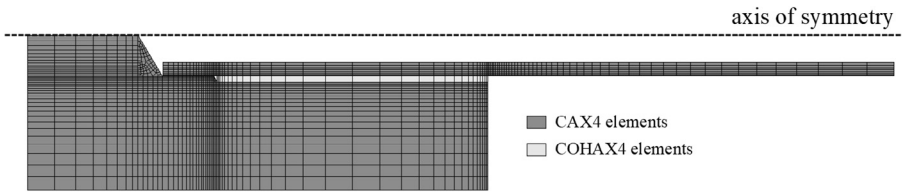


Fig. 5. Detail of the mesh for the FE model (without tapering of the adherends).

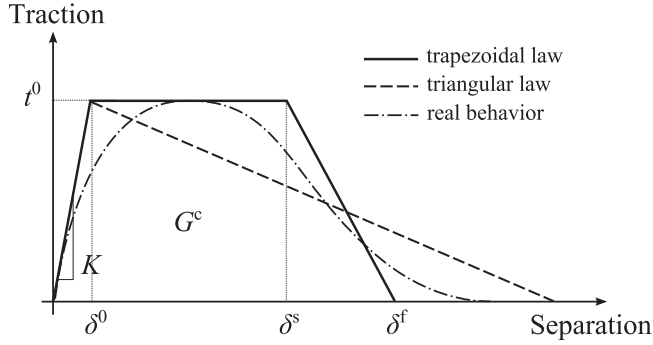


Fig. 6. Representation of triangular and trapezoidal traction-separation law shapes approximating the real behaviour of an adhesive.

by Eq. (3), where t^{und} is the cohesive traction that would have been reached without degradation.

$$t = (1 - d)t^{und} \quad (3)$$

Damage progresses until failure at δ^f , whose value in tension and shear is calculated by considering the area under the respective curve to be equal to its respective fracture toughness G^c . In the case of the trapezoidal law, a stress softening displacement δ^s is introduced. After damage initiation, the adhesive maintains its peak strength despite the increase of d , and the softening up to failure starts at δ^s . A simple predefined ratio of 0.8 was used between δ^s and δ^f , since the exact shape of the trapezoidal law has been shown to have a marginal impact on the joint strength [38,39]. It should be noted that Abaqus only provides the implementation of coupled degradation for the triangular and exponential laws. Consequently, when using a trapezoidal law, the tensile and shear behaviours of the cohesive elements are independent from damage initiation to failure. The values of the damage variable d with respect to the separation δ , in the constant stress and softening regions, were calculated from Eq. (4).

$$d = 1 - \frac{\delta^0}{\delta} \quad \text{if } \delta^0 < \delta < \delta^s$$

$$d = 1 - \frac{\delta^f - \delta}{K_{n,s} \delta (\delta^f - \delta^s)} t^0 \quad \text{if } \delta^s < \delta < \delta^f \quad (4)$$

Since K_n and K_s depend on the value of t_{adh} , new damage variable values must be calculated and implemented every time t_{adh} is modified in the model, which increases the total computational cost.

2.4. Specimens manufacturing and testing

In order to validate the numerical model, specimens were fabricated for different values of L_o , t_{adh} , t_{out} and d_{in} . The values considered were $L_o = 5, 10, 15$ and 20 mm, $t_{adh} = 0.1, 0.2, 0.3$ and 0.4 mm, $t_{out} = 2, 4, 6$ and 8 mm, and $d_{in} = 2, 3, 4$ and 5 mm. Each parameter was varied while the others were kept at constant “reference” values ($L_o = 10$ mm, $t_{adh} = 0.2$ mm, $t_{out} = 6$ mm and $d_{in} = 3$ mm, chosen arbitrarily among the two middle values of each parameter), resulting in 13 different configurations. No tapering was done on either adherend, and t_{in} was kept constant (0.5 mm). Five specimens were fabricated and tested for each configuration.

Due to the CFRP tubes having a relatively small diameter, it is difficult to grip them in the tensile machine without crushing them. Each



Fig. 7. Example of tubular joint specimen ($t_{out} = 2$ mm) in the testing apparatus.

specimen therefore consisted of one CFRP tube bonded at both ends to aluminium tubes enlarged at their extremities to be properly set in the tensile machine, as seen on Fig. 7. The specimens were fabricated via the following steps: (1) the adherends were degreased with acetone and manually abraded using sandpaper, (2) the CFRP tubes were inserted in the aluminium tubes and (3) the adhesive was injected in the overlap through an injection hole. A constant adhesive thickness and centring of the CFRP tube in the aluminium tube was ensured by a centring hole at the bottom of the overlap, drilled at a diameter equal to the CFRP tube’s diameter. To ensure a proper curing of the adhesive, the joined assembly was left for one week at room temperature. Testing of the specimens was carried out until failure in a tensile testing machine equipped with a load cell of 20 kN, with a controlled displacement rate of 1 mm/min and at room temperature.

During the tensile tests, the machine measured the crosshead displacement, which comprises the deformation of the specimen as well as the displacement induced by the deformation of the testing apparatus. The latter was measured by testing, in the same conditions, a short specimen made of steel (for a high stiffness resulting in negligible specimen deformations). The deformation of each joint specimen was then calculated by subtracting the deformation of the apparatus from the crosshead displacement. Furthermore, the deformation of the aluminium between the grip and the section analysed by the FE model (see Fig. 5) is assumed negligible.

3. Results and discussions

3.1. Numerical model validation

3.1.1. Joint strength prediction

All specimens were tested in tension failure, which was considered when the applied load reached a peak (P_f). In the sets of specimens with $L_o = 15$ mm and 20 mm, a high standard deviation between the failure loads is observed (550 N and 380 N from the average failure load, respectively). CT scan images of the specimens with $L_o = 15$ mm were taken after failure occurred (with the CFRP tubes still bonded to the aluminium tubes), in order to observe the adhesive layer and to try to

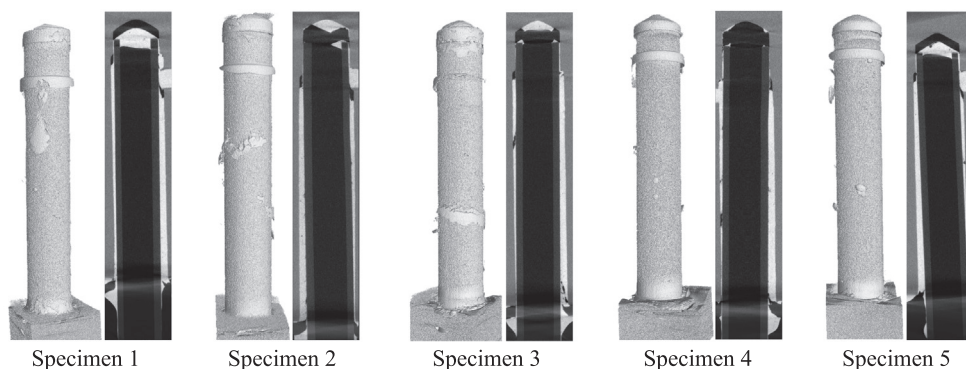


Fig. 8. CT scan images of the failed specimens with $L_o = 15$ mm: the 3D images show the air by making the other materials invisible, the 2D images show all materials (adhesive in white).

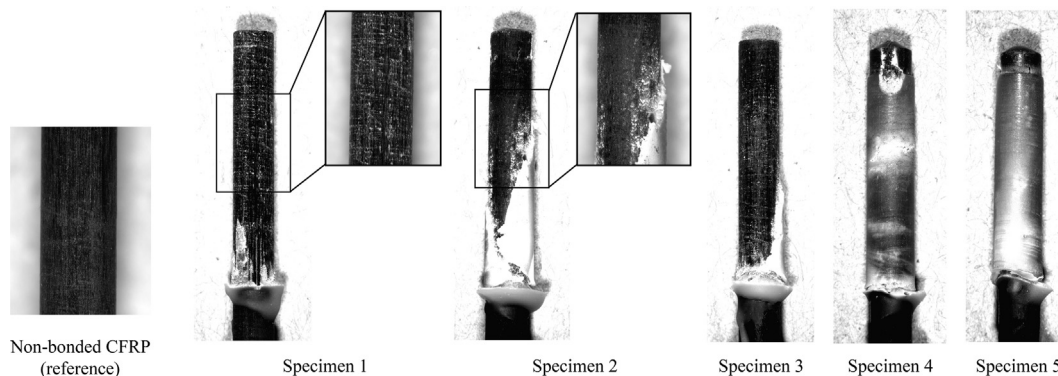


Fig. 9. CFRP tubes pulled out from the specimens with $L_o = 15$ mm.

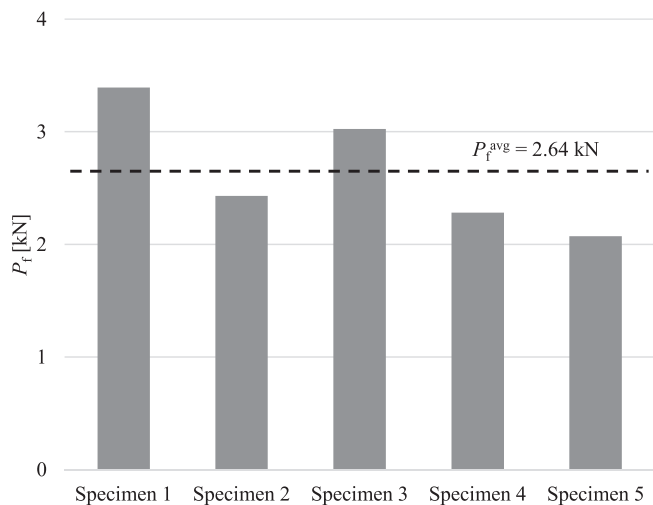


Fig. 10. Experimental failure loads P_f for the specimens with $L_o = 15$ mm.

understand the cause for this high failure load deviation. Fig. 8 shows the three-dimensional images of each failed joint, reconstructed from the CT scan images, along with two-dimensional images of the corresponding midsections. The 3D images have been set to show only the material with the lowest density (air), so that air bubbles in the adhesive can be easily visualized. Thus, the grey column visible in each image represents the air inside the CFRP tube, and the clearer “masses” show the air trapped within the adhesive layer. The 2D images depict the adhesive layer in white, the adherends in shades of grey and the air in black. Fig. 9 shows the CFRP tubes after they were completely pulled out from the aluminium tubes. The surface of a non-bonded CFRP tube is provided as a reference, to be compared with the surfaces of the

pulled-out tubes. Fig. 10 shows the respective failure loads of the specimens shown in Figs. 8 and 9.

The pulled-out CFRP tubes shown in Fig. 9 reveal that the specimens with the lowest failure loads (specimens 4 and 5) are still entirely covered by the adhesive layer, suggesting that the failure did not happen within the adhesive but at the interface between the adhesive and the aluminium. Conversely, the specimens with the highest failure loads (specimens 1 and 3) show adhesive only at the loaded end of the overlap, suggesting a cohesive failure originating from this location. It can be concluded that one cause for the high deviation in failure loads is an improper pre-treatment of the aluminium adherends. The bottom of the aluminium tubes was difficult to reach, which might have led to an insufficient abrasion in this area, with a higher risk of improper abrasion the higher the overlap length. It explains why the highest deviations were observed for the specimen sets with the highest overlap lengths. On specimen 2, an important amount of adhesive is still present, and the surface of the CFRP tube looks like it was not properly bonded, suggesting an improper pre-treatment of the CFRP tube at this location. For future similar tests, the use of a more homogeneous pre-treatment technique on the aluminium adherends, such as chemical etching, is advised.

Another possible cause for the high deviation is a misalignment of the adherends. The 2D images in Fig. 8 show that, despite the specimens being assembled in a fixture designed to keep the tubes centred, the CFRP tubes are off-centre close to the open end of the overlap, resulting in an uneven adhesive thickness in this area. This misalignment being present in all of the five specimens scanned, it is difficult to gauge its impact on the failure load of the joints. Although previous studies have shown the robustness of tubular joints to manufacturing defects [17,18], the authors advise the use of a different centring method, such as inserting nylon threads as spacers between the adherends. Similarly, air bubbles of various sizes can be observed in the 3D images of the

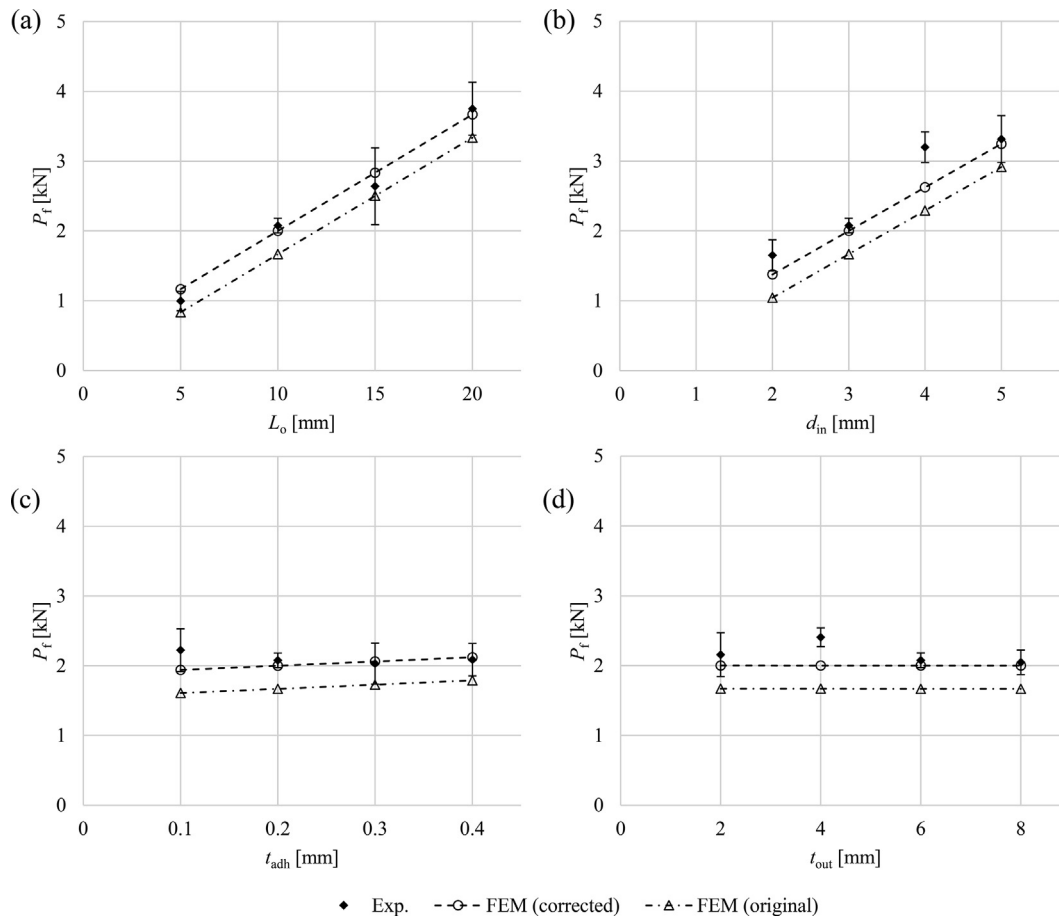


Fig. 11. Experimental and predicted P_f for different values of L_o (a), d_{in} (b), t_{adh} (c) and t_{out} (d).

specimens with no apparent relationship between the size of the bubbles and the failure loads of the specimens.

The 2D images in Fig. 8 also reveal that, during the injection of the adhesive in the overlap, some of it went in the centring hole between the CFRP and the aluminium. It might have caused the joint strength obtained experimentally to be higher than the one predicted by the numerical models, due to the extra 2 mm of overlap it created. In order to verify this observation, a “corrected” numerical model was created by replacing the centring hole with an extra 2 mm length of adhesive. The comparison of the experimental failure loads with the predictions made by the original and corrected models are presented on Fig. 11. The original model under-predicts the failure loads by 19.9% on average, against 4.2% for the corrected model, which validates the use of the corrected model to predict the strength of tubular joints. In the following sections, the corrected values of L_o (adding 2 mm of adhesive length) and the results from the corrected model are used.

3.1.2. Damage analysis

Fig. 12 reports the load-displacement curves obtained experimentally for the reference specimens, along with the FEM simulation from the corresponding model (displacement values are doubled for the numerical results, since the model represents one half of a specimen). The good agreement observed between the experimental and numerical curves validates the assumptions made in Section 2.4 about the measured displacements. The displacements applied in the simulation when the joint reaches its peak load and when it starts softening are labelled d_p and d_s , respectively. To explain the shape of the load-displacement curve given by the numerical simulation, the damage variable d and the shear stress τ_{xy} (normalized by τ_r) along the adhesive overlap are plotted for different values of applied displacement around d_p and d_s

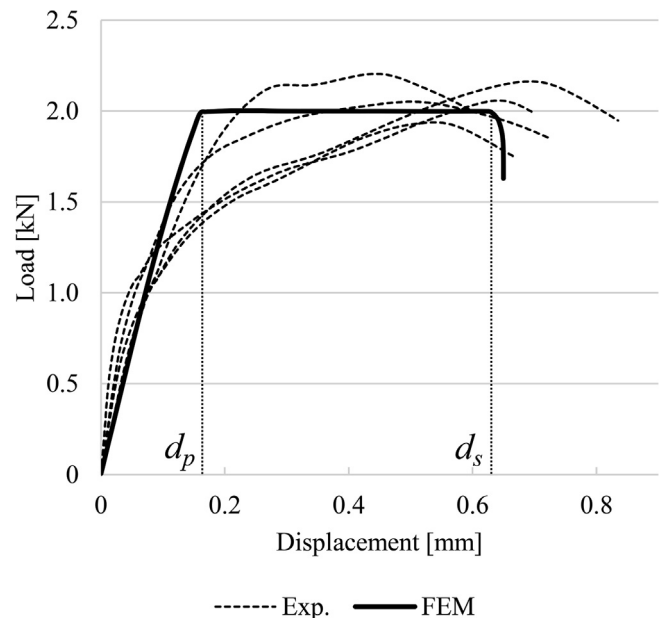


Fig. 12. Numerical and experimental load-displacement curves for the reference specimens ($L_o = 12$ mm).

(Fig. 13). It shows that damage initiates at the end of the overlap when the adhesive reaches its peak stress at this location (see the 42% d_p curves on Fig. 13). As the applied displacement increases, the shear stresses are redistributed to the undamaged parts of the overlap and the load applied on the joint increases. The load reaches a peak when the

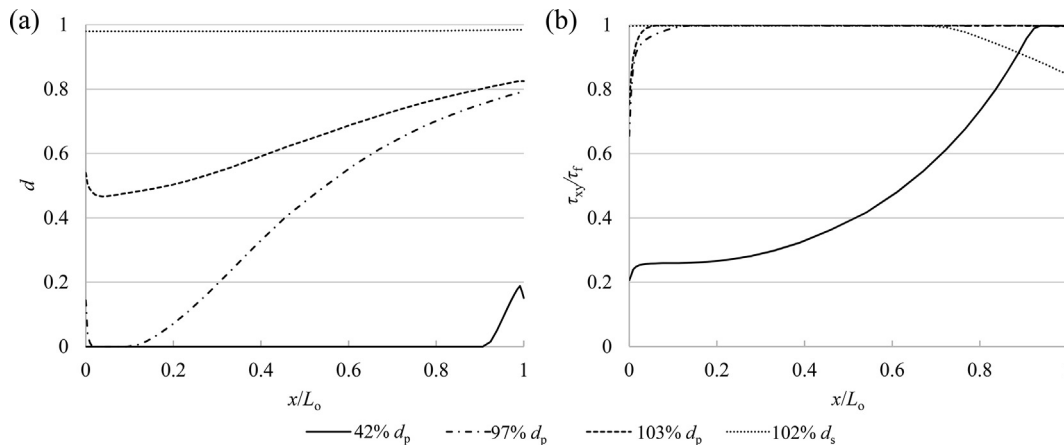


Fig. 13. Damage variable (a) and normalized shear stress (b) along the adhesive overlap of the joint with $L_o = 12$ mm, where d_p and d_s are the displacements applied when the joint reaches its peak load and when it starts softening, respectively.

entire overlap has initiated damage (97% d_p and 103% d_p curves) and the stresses cannot be redistributed anymore. The applied load stays at this peak value when the applied displacement increases further, and starts dropping when the adhesive starts softening (102% d_s curves), i.e. when $d = 0.981$ (calculated using the equations defined in Section 2.3).

The distinct separation values δ^o and δ^s of the trapezoidal law result in a load–displacement curve with similarly distinct displacements d_p and d_s when the peak load is reached and when the load starts dropping. In contrast, the real traction–separation law for an adhesive is non-linear, i.e. it does not feature such distinct points delimitating linear zones, as shown in Fig. 6. It explains why the load–displacement curves obtained experimentally have a continuous shape instead of the trapezoidal one obtained numerically. This is a limitation inherent to the approximation of the traction–separation law, but given the good accuracy of the strength predictions obtained numerically, this approximation is judged acceptable for the purpose of this work.

3.2. Influence of the design parameters

3.2.1. Overlap length and inner tube diameter

As observed in Fig. 11, the overlap length (L_o) and inner tube diameter (d_{in}) are the parameters with the highest influence on the joint strength. The corrected model was used to predict the strength of joints with several combinations of L_o and d_{in} , and the results are presented in Fig. 14. The results show that a limit value of L_o exists after which P_f

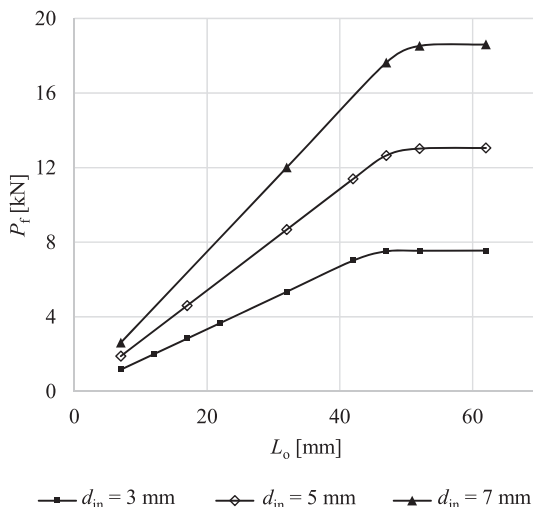


Fig. 14. Failure load for different values of L_o and d_{in} .

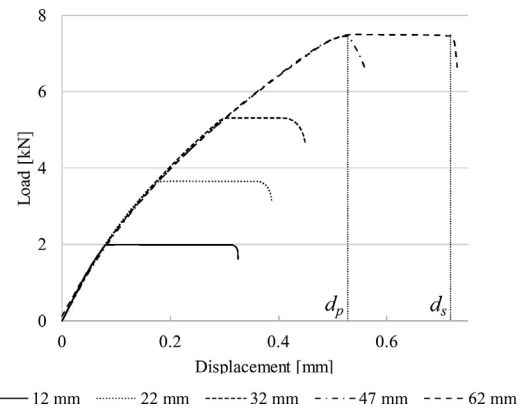


Fig. 15. Load-displacement curves for different values of L_o , where d_p and d_s are indicated for $L_o = 62$ mm.

does not increase further, and that this limit slightly increases with d_{in} . On the other hand, no limit value of d_{in} was observed. Fig. 15 shows the load-displacement curves obtained numerically for $d_{in} = 3$ mm and different values of L_o .

The part of the curve where the joint maintains its peak load (the flat part) becomes shorter as L_o increases, and grows longer again after the limit value of L_o is reached. In order to explain this behaviour, a damage analysis similar to the one made in Section 3.1.2 is made for the model with $L_o = 62$ mm (Fig. 16). Similarly to the joint with $L_o = 12$ mm, after damage has initiated at the end of the overlap (see the 8% d_p curves on Fig. 16), the stresses are redistributed and the load applied to the joint keeps increasing. However, when the adhesive starts failing at the end of the overlap and the peak stress zone stops growing longer (89% d_p and 101% d_p curves), the load reaches P_f , even though the rest of the overlap has not initiated damage yet. The load starts dropping when damage has been initiated in the entire overlap (99% d_s and 101% d_s curves) and the peak stress zone becomes shorter due to the adhesive gradually failing. In summary, before a certain limit value of L_o (around 47 mm in this case) there is a proportional increase of P_f with L_o , due to the applied load reaching P_f only when the entire overlap has initiated damage. Above this limit value of L_o , the applied load reaches P_f when the peak stress zone cannot get any longer and the adhesive starts failing at one end of the overlap. The length of the peak stress zone being independent from L_o , further increasing L_o does not cause P_f to increase anymore.

3.2.2. Adhesive and adherends thickness

Fig. 11c shows that the adhesive thickness (t_{adh}) has no significant

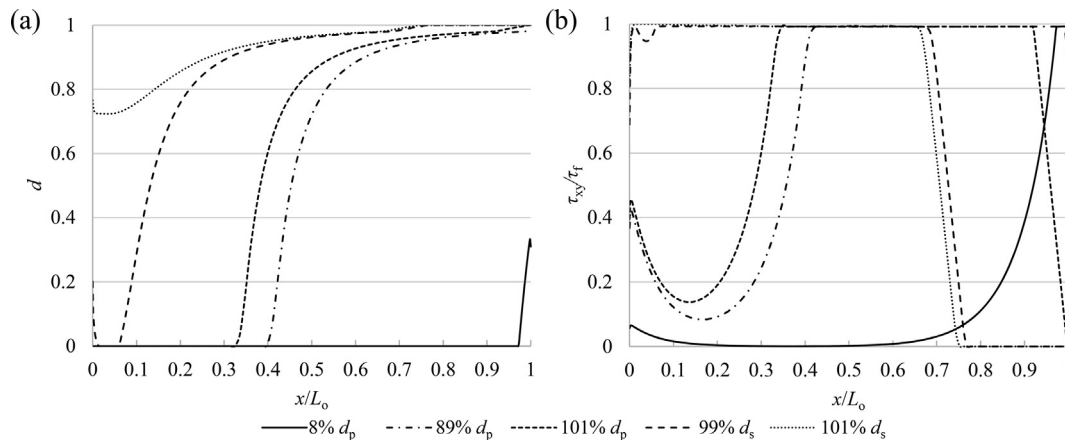


Fig. 16. Damage variable (a) and normalized shear stress (b) along the adhesive overlap of the joint with $L_o = 62$ mm, where d_p and d_s are the displacements applied when the joint reaches its peak load and when it starts softening, respectively.

influence on the failure load of the joint, compared to the influence of L_o and d_{in} . Variations of t_{adh} also have a marginal influence on the total weight of the joint, and require extra computational time since a new traction-separation law must be computed for each new value of t_{adh} . Therefore considering the adhesive thickness as an optimization variable in the future is judged unnecessary, and the choice of a constant value is preferred.

Variations of the inner and outer tubes thickness (t_{in} and t_{out} , respectively) have an influence on P_f for high overlap lengths. Fig. 17 shows the failure loads obtained numerically for different values of L_o , t_{in} and t_{out} . Reducing t_{out} results in an increase of P_f for higher overlap lengths, while reducing t_{in} results in a decrease of P_f . This is due to the influence of the adherends geometry on the shear stress distribution along the adhesive overlap (see Fig. 18 for the case of $L_o = 62$ mm). Reducing t_{out} contributes to reducing the stiffness imbalance between the adherends, causing a better shear stress and damage distribution. A different distribution has no influence on P_f for short overlap lengths, since in that case P_f is reached when the entire overlap has initiated damage. However, for higher overlap lengths, P_f is reached when one end of the overlap (the one with the highest peak stresses) starts failing, regardless of the amount of damage in the rest of the overlap. Lower shear stresses at this location cause the load required for the adhesive to fail to be higher, which results in a higher P_f plateau (as seen in Fig. 17). Conversely, reducing t_{in} contributes to increasing the stiffness imbalance, which results in a lower P_f plateau. Additionally, there are lower limits on t_{out} and t_{in} , under which the applied load causes the

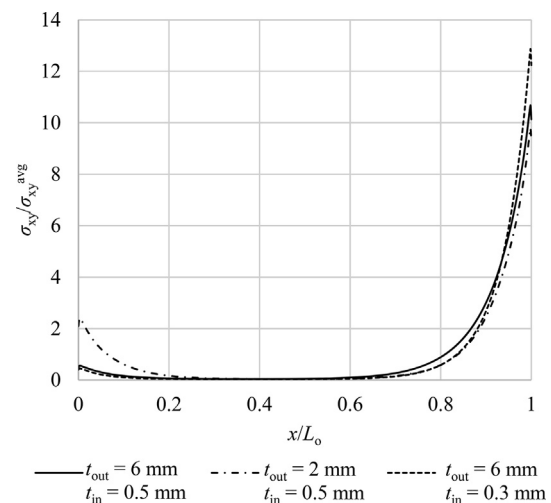


Fig. 18. Normalized shear stress distribution along the adhesive overlap for $L_o = 62$ mm and different values of t_{in} and t_{out} (stress values obtained for the same applied load).

adherent to fail before the adhesive layer.

3.2.3. Taper length

As with the adherends thickness, the inner and outer tubes taper lengths (l_{in} and l_{out} , respectively) have an influence on P_f for high overlap lengths. Fig. 19 shows the failure loads obtained numerically for different values of l_{in} and l_{out} , for $L_o = 7$ and 62 mm. To ensure that the tapering of an adherend does not reduce its thickness (given by t_{in} or t_{out}), its length cannot exceed L_o . An outer tube thickness of $t_{out} = 3$ mm was used for the results shown in Fig. 19. The results for $L_o = 7$ mm show no influence of the tapering on P_f . For $L_o = 62$ mm, high values of l_{out} result in a higher P_f , while high values of l_{in} result in a lower P_f . As explained in Section 3.2.2, the variation of the stiffness imbalance between the adherends, here caused by the tapering, results in a variation of the stress distribution (shown in Fig. 20 for $L_o = 62$ mm). Strength improvements are obtained when the taper length of the stiffest adherend is increased, as shown with the increase in P_f obtained with a high l_{out} . On the other hand, tapering the least stiff adherend further increases the stiffness imbalance, resulting in a decrease of P_f .

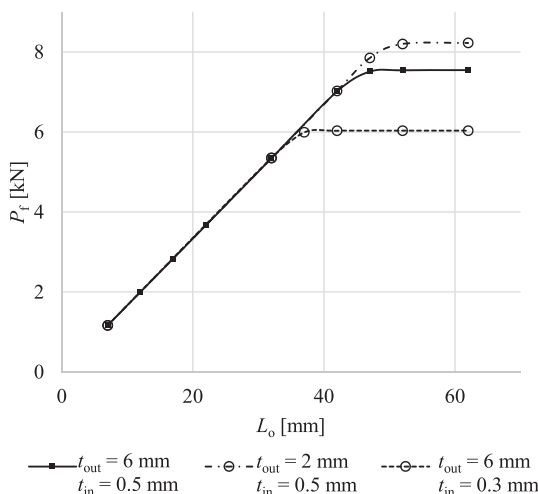


Fig. 17. Failure load for different values of L_o , t_{in} and t_{out} .

4. Conclusions

In this work, tubular joints consisting of CFRP tubes adhesively

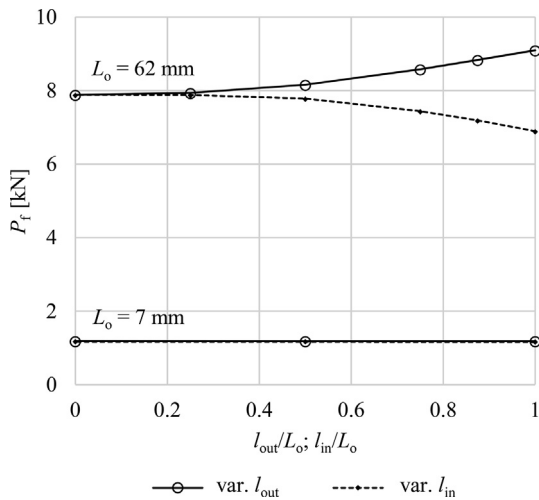


Fig. 19. Failure load for $L_0 = 7$ and 62 mm, $t_{out} = 3$ mm and different values of l_{in} and l_{out} .

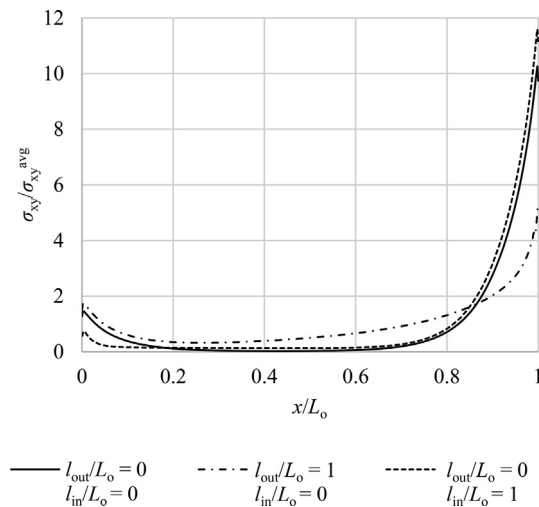


Fig. 20. Normalized shear stress distribution along the adhesive overlap for $L_0 = 62$ mm, $t_{out} = 3$ mm and different values of l_{in} and l_{out} (stress values obtained for the same applied load).

bonded inside aluminium tubes were modelled for different values of overlap length (L_0), adhesive thickness (t_{adh}), inner tube diameter (d_{in}), inner and outer tubes thickness (t_{in} and t_{out} , respectively), and inner and outer tubes taper lengths (l_{in} and l_{out} , respectively), to study the influence of these parameters on the joint strength and weight. The numerical model used a CZM formulation with a trapezoidal traction-separation law for the adhesive layer, and experimental tests were carried to validate it. CT scan images of failed specimens showed that manufacturing defects, such as air bubbles in the adhesive layer or a misalignment of the adherends, do not have an apparent influence on the joint strength. However, it highlighted cases of improper pre-treatment of the adherends, leading to the premature failure of some specimens. This issue was attributed to the pre-treatment technique used (mechanical abrasion) having a higher risk of being non-uniform for longer overlaps, and the authors recommend the use of a more homogeneous technique such as chemical etching. Nevertheless, the failure loads predicted by the model were in good agreement with the ones obtained experimentally, validating the use of CZM as a design tool for this type of joint.

The parametric study showed that the joint strength increases significantly with L_0 and d_{in} , with a limit on L_0 after which the strength stops increasing. A damage analysis showed that the initial increase of

the failure load (P_f) with L_0 is due to the joint reaching P_f when the entire adhesive overlap has initiated damage. Above a certain limit on L_0 , the adhesive layer starts failing before damage has initiated in the entire overlap, preventing P_f from increasing further with L_0 . The adherends thickness (t_{in} and t_{out}) and taper lengths (l_{in} and l_{out}) have an influence on the uniformity of the shear stress distribution along the adhesive overlap, which in turn influences P_f for high overlap lengths. Furthermore, there are lower limits on t_{in} and t_{out} , under which the applied load can cause the adherends to fail before the adhesive layer. In addition to their influence of the joint strength, these six parameter also have a significant influence on the total weight, which make them important variables to consider in a future optimization process. On the other hand, the adhesive thickness t_{adh} has only a marginal influence on the joint strength and weight, and the extra computational time required when varying this parameter makes the choice of a fixed value preferable.

Funding

This research is funded by the Faculty of Aerospace Engineering of the Delft University of Technology.

Data availability Statement:

The processed data required to reproduce these findings are available to download from: <http://doi.org/10.4121/uuid:92773369-5dcca1-9f47-5d3a5336cc2e>

CRediT authorship contribution statement

Nicolas P. Lavalette: Conceptualization, Methodology, Software, Validation, Formal analysis, Investigation, Data curation, Writing - original draft, Visualization. **Otto K. Bergsma:** Conceptualization, Writing - review & editing, Supervision. **Dimitrios Zarouchas:** Writing - review & editing, Supervision. **Rinze Benedictus:** Supervision.

Declaration of Competing Interest

The authors declare that they have no known competing financial interests or personal relationships that could have appeared to influence the work reported in this paper.

Appendix A. Supplementary data

Supplementary data to this article can be found online at <https://doi.org/10.1016/j.compstruct.2020.112077>.

References

- [1] Weaver TJ, Jensen DW. Mechanical Characterization of a Graphite/Epoxy IsoTruss. *J Aerosp Eng* 2002;13:23–35. [https://doi.org/10.1061/\(asce\)0893-1321\(2000\)13:1\(23\)](https://doi.org/10.1061/(asce)0893-1321(2000)13:1(23)).
- [2] Woods BKS, Hill I, Friswell MI. Ultra-efficient wound composite truss structures. *Compos Part A Appl Sci Manuf* 2016;90:111–24. <https://doi.org/10.1016/j.compositesa.2016.06.022>.
- [3] Xu J, Wu Y, Gao X, Wu H, Nutt S, Yin S. Design of composite lattice materials combined with fabrication approaches. *J Compos Mater* 2019;53:393–404. <https://doi.org/10.1177/0021998318785710>.
- [4] Ascione F, Lamberti M, Razaqpur AG, Spadea S. Strength and stiffness of adhesively bonded GFRP beam-column moment resisting connections. *Compos Struct* 2017. <https://doi.org/10.1016/j.compstruct.2016.11.021>.
- [5] Ascione F, Lamberti M, Razaqpur AG, Spadea S, Malagic M. Pseudo-ductile failure of adhesively joined GFRP beam-column connections: An experimental and numerical investigation. *Compos Struct* 2018. <https://doi.org/10.1016/j.compstruct.2018.05.104>.
- [6] Razaqpur AG, Ascione F, Lamberti M, Spadea S, Malagic M. GFRP hollow column to built-up beam adhesive connection: Mechanical behaviour under quasi-static, cyclic and fatigue loading. *Compos Struct* 2019. <https://doi.org/10.1016/j.compstruct.2019.111069>.
- [7] Lavalette NP, Bergsma OK, Zarouchas D, Benedictus R. Comparative study of adhesive joint designs for composite trusses based on numerical models. *Appl Adhes*

- Sci 2017;5:20. <https://doi.org/10.1186/s40563-017-0100-1>.
- [8] Neto JABP, Campilho RDSG, da Silva LFM. Parametric study of adhesive joints with composites. *Int J Adhes Adhes* 2012;37:96–101. <https://doi.org/10.1016/j.ijadhadh.2012.01.019>.
- [9] Ozel A, Yazici B, Akpinar S, Aydin MD, Temiz Ş. A study on the strength of adhesively bonded joints with different adherends. *Compos Part B Eng* 2014. <https://doi.org/10.1016/j.compositesb.2014.03.001>.
- [10] Gültekin K, Akpinar S, Özel A. The effect of the adherend width on the strength of adhesively bonded single-lap joint: Experimental and numerical analysis. *Compos Part B Eng* 2014. <https://doi.org/10.1016/j.compositesb.2014.01.022>.
- [11] Banea MD, da Silva LFM, Carbas R, Campilho RDSG. Effect of material on the mechanical behaviour of adhesive joints for the automotive industry. *J Adhes Sci Technol* 2016;31:663–76. <https://doi.org/10.1080/01694243.2016.1229842>.
- [12] Barbosa DR, Campilho RDSG, Rocha RJB, Ferreira LRF. Experimental and numerical assessment of tensile loaded tubular adhesive joints. *Proc Inst Mech Eng Part L J Mater Des Appl* 2018;1–13. <https://doi.org/10.1177/1464420718808543>.
- [13] Li J, Yan Y, Zhang T, Liang Z. Experimental study of adhesively bonded CFRP joints subjected to tensile loads. *Int J Adhes Adhes* 2015. <https://doi.org/10.1016/j.ijadhadh.2014.11.001>.
- [14] Bouchikhi AS, Megueni A, Gouasmi S, Boukouloua FB. Effect of mixed adhesive joints and tapered plate on stresses in retrofitted beams bonded with a fiber-reinforced polymer plate. *Mater Des* 2013. <https://doi.org/10.1016/j.matdes.2013.03.052>.
- [15] Labbé S, Drouet JM. A multi-objective optimization procedure for bonded tubular-lap joints subjected to axial loading. *Int J Adhes Adhes* 2012. <https://doi.org/10.1016/j.ijadhadh.2011.09.005>.
- [16] Ferreira LRF, Campilho RDSG, Rocha RJB, Barbosa DR. Geometrical and material optimization of tensile loaded tubular adhesive joints using cohesive zone modelling. *J Adhes* 2019;00:1–25. <https://doi.org/10.1080/00218464.2018.1551136>.
- [17] Kohl D, Ratsch N, Böhm S, Voß M, Kaufmann M, Vallée T. Influence of manufacturing methods and imperfections on the load capacity of glued-in rods. *J Adhes* 2018;00:1–22. <https://doi.org/10.1080/00218464.2018.1508351>.
- [18] Gonzales E, Tannert T, Vallee T. The impact of defects on the capacity of timber joints with glued-in rods. *Int J Adhes Adhes* 2016. <https://doi.org/10.1016/j.ijadhadh.2015.11.002>.
- [19] Castagnetti D, Spaggiari A, Dragoni E. Effect of bondline thickness on the static strength of structural adhesives under nearly-homogeneous shear stresses. *J Adhes* 2011;87:780–803. <https://doi.org/10.1080/00218464.2011.597309>.
- [20] Budhe S, Banea MD, de Barros S, da Silva LFM. An updated review of adhesively bonded joints in composite materials. *Int J Adhes Adhes* 2016;72:50. <https://doi.org/10.1016/j.ijadhadh.2016.10.010>.
- [21] Fernandes TAB, Campilho RDSG, Banea MD, da Silva LFM. Adhesive Selection for Single Lap Bonded Joints: Experimentation and Advanced Techniques for Strength Prediction. *J Adhes* 2015;91:841–62. <https://doi.org/10.1080/00218464.2014.994703>.
- [22] Campilho RDSG, Banea MD, Neto JABP, da Silva LFM. Modelling adhesive joints with cohesive zone models: Effect of the cohesive law shape of the adhesive layer. *Int J Adhes Adhes* 2013;44:48–56. <https://doi.org/10.1016/j.ijadhadh.2013.02.006>.
- [23] Ribeiro TEA, Campilho RDSG, da Silva LFM, Goglio L. Damage analysis of composite-aluminium adhesively-bonded single-lap joints. *Compos Struct* 2016;136:25–33. <https://doi.org/10.1016/j.compstruct.2015.09.054>.
- [24] Campilho RDSG, Pinto AMG, Banea MD, Silva RF, da Silva LFM. Strength improvement of adhesively-bonded joints using a reverse-bent geometry. *J Adhes Sci Technol* 2011;25:2351–68. <https://doi.org/10.1163/016942411X580081>.
- [25] Dragoni E, Goglio L. Adhesive stresses in axially-loaded tubular bonded joints - Part I: Critical review and finite element assessment of published models. *Int J Adhes Adhes* 2013. <https://doi.org/10.1016/j.ijadhadh.2013.09.009>.
- [26] Nunes SLS, Campilho RDSG, Da Silva FJG, De Sousa CCRG, Fernandes TAB, Banea MD, et al. Comparative failure assessment of single and double lap joints with varying adhesive systems. *J Adhes* 2016. <https://doi.org/10.1080/00218464.2015.1103227>.
- [27] Harris JA, Adams RA. Strength prediction of bonded single lap joints by non-linear finite element methods. *Int J Adhes Adhes* 1984;4:65–78. [https://doi.org/10.1016/0143-7496\(84\)90103-9](https://doi.org/10.1016/0143-7496(84)90103-9).
- [28] Crocombe AD. Global yielding as a failure criterion for bonded joints. *Int J Adhes Adhes* 1989;9:145–53. [https://doi.org/10.1016/0143-7496\(89\)90110-3](https://doi.org/10.1016/0143-7496(89)90110-3).
- [29] da Silva LFM, Campilho RDSG. Advances in numerical modelling of adhesive joints. *SpringerBriefs Appl. Sci. Technol.* 2012:1–93. https://doi.org/10.1007/978-3-642-23608-2_1.
- [30] Hu XF, Chen BY, Tirvaudey M, Tan VBC, Tay TE. Integrated XFEM-CE analysis of delamination migration in multi-directional composite laminates. *Compos Part A Appl Sci Manuf* 2016. <https://doi.org/10.1016/j.compositesa.2016.07.007>.
- [31] van Dongen B, van Oostrum A, Zarouchas D. A blended continuum damage and fracture mechanics method for progressive damage analysis of composite structures using XFEM. *Compos Struct* 2018. <https://doi.org/10.1016/j.compstruct.2017.10.007>.
- [32] Lamberti M, Maurel-Pantel A, Ascione F, Lebon F. Influence of web/flange reinforcement on the GFRP bonded beams mechanical response: A comparison with experimental results and a numerical prediction. *Compos Struct* 2016. <https://doi.org/10.1016/j.compstruct.2016.03.043>.
- [33] Campilho RDSG, Banea MD, Pinto AMG, da Silva LFM, de Jesus AMP. Strength prediction of single- and double-lap joints by standard and extended finite element modelling. *Int J Adhes Adhes* 2011;31:363–72. <https://doi.org/10.1016/j.ijadhadh.2010.09.008>.
- [34] Campilho RDSG, de Moura MFSF, Ramantani DA, Morais JLL, Domingues JJMS. Buckling Behaviour of Carbon-Epoxy Adhesively-Bonded Scarf Repairs. *J Adhes Sci Technol* 2009;23:1493–513. <https://doi.org/10.1163/156856109X433045>.
- [35] Carlberger T, Stigh U. Influence of layer thickness on cohesive properties of an epoxy-based adhesive-an experimental study. *J Adhes* 2010;86:814–33. <https://doi.org/10.1080/00218464.2010.498718>.
- [36] de Barros S, Champaney L, Valoroso N. Numerical simulations of crack propagation tests in adhesive bonded joints. *Lat Am J Solids Struct* 2012;9:339–51. <https://doi.org/10.1590/s1679-78252012000300002>.
- [37] Dassault Systemes. Abaqus 2017 Documentation n.d.
- [38] Tvergaard V, Hutchinson JW. The relation between crack growth resistance and fracture process parameters in elastic-plastic solids. *J Mech Phys Solids* 1992. [https://doi.org/10.1016/0022-5096\(92\)90020-3](https://doi.org/10.1016/0022-5096(92)90020-3).
- [39] Yang QD, Thouless MD, Ward SM. Numerical simulations of adhesively-bonded beams failing with extensive plastic deformation. *J Mech Phys Solids* 1999. [https://doi.org/10.1016/S0022-5096\(98\)00101-X](https://doi.org/10.1016/S0022-5096(98)00101-X).